Biomech Model Mechanobiol (2017) 16:395–410
DOI 10.1007/s10237-016-0824-z

ORIGINAL PAPER

Computer modelling of bone's adaptation: the role of normal strain, shear strain and fluid flow

Abhishek Kumar Tiwari[1] · **Jitendra Prasad**[1]

Received: 12 January 2016 / Accepted: 8 June 2016 / Published online: 1 September 2016

Abstract Bone loss is a serious health problem. In vivo studies have found that mechanical stimulation may inhibit bone loss as elevated strain in bone induces osteogenesis, i.e. new bone formation. However, the exact relationship between mechanical environment and osteogenesis is less clear. Normal strain is considered as a prime stimulus of osteogenic activity; however, there are some instances in the literature where osteogenesis is observed in the vicinity of minimal normal strain, specifically near the neutral axis of bending in long bones. It suggests that osteogenesis may also be induced by other or secondary components of mechanical environment such as shear strain or canalicular fluid flow. As it is evident from the literature, shear strain and fluid flow can be potent stimuli of osteogenesis. This study presents a computational model to investigate the roles of these stimuli in bone adaptation. The model assumes that bone formation rate is roughly proportional to the normal, shear and fluid shear strain energy density above their osteogenic thresholds. In vivo osteogenesis due to cyclic cantilever bending of a murine tibia has been simulated. The model predicts results close to experimental findings when normal strain, and shear strain or fluid shear were combined. This study also gives a new perspective on the relation between osteogenic potential of micro-level fluid shear and that of macro-level bending shear. Attempts to establish such relations among the components of mechanical environment and corresponding osteogenesis may ultimately aid in the development of effective approaches to mitigating bone loss.

✉ Jitendra Prasad
jprasad@iitrpr.ac.in

[1] School of Mechanical Materials and Energy Engineering, Indian Institute of Technology Ropar, Room No. 303, Nangal Road, Rupnagar, Punjab 140001, India

Keywords Bone Loss · Osteogenesis · Normal Strain · Shear Strain · Fluid Flow

List of symbols

ε_i	normal strain at surface coordinate 'i'
M	bending moment
y_i	distance from the neutral axis to surface coordinate 'i'
E	Young's modulus of the bone
I	area moment of inertia
γ_i	shear strain at surface coordinate 'i'
V	vertical shear force
Q_i	first moment of area
t_i	width of the section at point 'i'
P_{steady}	steady-state response of the pore pressure
B	relative compressibility constant or Skempton coefficient
υ_u	Poisson's ratio of the solid bone matrix under undrained conditions
a	thickness of the cortex
y^*	dimensionless length parameter
t^*	dimensionless time parameter
Ω	dimensionless frequency parameter
t	time
c	diffusion coefficient
ω	angular frequency ($=2\pi f$)
υ	Poisson's ratio of the bone
H	dimensionless stress coefficient
S_i	fluid shear stress at surface coordinate 'i'
b_o	radius of the canaliculus
a_o	radius of the cell process
λ	dimensionless length ratio ($=b_o/\sqrt{k_p}$)
k_p	Darcy's law permeability constant

I_o	modified Bessel function of the first kind
K_o	modified Bessel function of the third kind
q	the ratio of the radius of the canaliculus, b_o, to the radius of the cell process, a_o,$(=b_o/a_o)$
$U_i^{\varepsilon}, U_i^{\gamma}, U_i^{s}$	strain energy density (SED) due to the normal strain, the shear strain and the fluid shear, respectively, at surface coordinate 'i'
$U_{ref}^{\varepsilon}, U_{ref}^{\gamma}, U_{ref}^{s}$	reference SED for normal strain, shear strain and fluid shear, respectively.
C	bone's surface remodelling rate coefficient
G	shear modulus of the bone
G_{osc}	shear modulus of the osteocyte
Δ_i	natural bone growth rate at surface coordinate 'i'

1 Introduction

Metabolic bone disorders such as osteoporosis or bone/muscle disuse cause bone loss which ultimately leads to severe fractures in weight-bearing bones (Dirschl et al. 1997; Maimoun et al. 2006; Lau and Guo 2011; Vico et al. 2000). Several in vivo studies have shown that a dynamic loading on bone may effectively inhibit bone resorption as it encourages new bone formation at the sites of peak strain magnitude (Rubin and Lanyon 1985; Hillam and Skerry 1995; Inman et al. 1999; Rubin et al. 2003; Shackelford 2004). Normal strain is believed to act as a principal stimulus of osteogenesis (Turner et al. 1994; Kotha et al. 2004; De Souza et al. 2005; Sample et al. 2010; Moustafa et al. 2012). However, based on a site-specific comparative analysis between the new bone distribution reported in several in vivo studies (such as Gross et al. 1997; Judex et al. 1997; Mosley et al. 1997; Srinivasan et al. 2002; LaMothe 2004; Zhang 2006; Kuruvilla et al. 2008; Matsumoto et al. 2008; Roberts et al. 2009; Lynch et al. 2011; Sakai et al. 2011; Weatherholt et al. 2013; Wallace et al. 2014; Birkhold et al. 2014) and the corresponding strain distribution, especially the position of neutral axis, reported in the same (Judex et al. 1997; Mosley et al. 1997; Zhang 2006; Matsumoto et al. 2008; Wallace et al. 2014) or other studies (Akhter et al. 1992; Srinivasan and Gross 1999; Srinivasan et al. 2013; Willie et al. 2013; Wagner et al. 2013; Patel et al. 2014; Yang et al. 2014; Razi et al. 2015), we find several instances where new bone formation occurs even in the absence of normal strain, specifically near neutral axis of bending in long bones. For example, an in vivo study on murine tibiae of female C57Bl/6J mice (10 weeks old) subjected to cantilever bending of 0.5 N for 500 loading cycles at 1 Hz led to osteogenesis away from as well as near the neutral axis; thus, the normal strain alone was unable to explain the site-specificity of new bone formation (Srinivasan et al. 2002). In that study, it can also be seen that new bone formation in the case of 0.5 N loading is more than that in 0.25 N loading group, site-specifically near the neutral axis at the endocortical surface, and it was also reported that no significant difference in new bone distribution was noticed between the control and 0.25 N loading groups. Hence, osteogenesis is mostly due to mechanical loading although natural growth is slightly present at endocortical surface (compare Fig. 1c with Fig. 3a). As such, the mid-diaphyseal histological section reported in Srinivasan et al. (2002) represents a typical new bone distribution for cantilever loading case which can be observed in several similar in vivo studies (Srinivasan 2003; LaMothe 2004; Srinivasan et al. 2010). Osteogenesis was similarly enhanced significantly in loaded limb as compared to natural bone growth in intact limb, in most of the above-cited studies. These studies were done on 10- to 16-week-old mice, which are equivalent to 18.4- to 24-year-old humans. This age group has been widely considered suitable in the literature to study bone's adaptation as the active bone growth decreases by the age of 16 weeks (Beamer et al. 1996; Sheng et al. 1999; Lee et al. 2002; Ferguson et al. 2003; Somerville et al. 2004; Wergedal et al. 2005; Flurkey et al. 2007; Main et al. 2010; Sakai et al. 2011). New bone formation near minimal strain sites has also been observed in fully adult mice (Srinivasan et al. 2002, 2010), growing rats (Mosley et al. 1997), juvenile sheep (Wallace et al. 2014) and adult turkey (Judex et al. 1997).

This work presents a computational study that attempts to investigate and explain new bone formation at minimal strain sites. A number of computational models are already available in the literature which can predict and/or simulate site-specific new bone formation (Huiskes et al. 1987; Brown et al. 1990; Fridez et al. 1998; Levenston et al. 1998; Taylor et al. 2003; Ausk et al. 2006; Martínez and Cerrolaza 2006; Chennimalai Kumar et al. 2009; Florio and Narh 2012). These models assume normal strain as a sole primary stimulus for osteogenesis and hence fall short to simulate those experiments where osteogenic activities are observed around minimal strain magnitude. Lack of spatial correlation between locations of new bone formation and that of elevated normal strain proposes that osteogenesis may be driven by secondary components of induced mechanical environment such as bending-induced shear stresses and canalicular fluid flow, which may be potent stimuli of osteogenesis near minimal strain sites (Thompson 1942; Srinivasan and Gross 2000; Burr et al. 2002). In fact, several in vivo and in vitro studies have explained the role of shear strain (De Margerie et al. 2005; Skedros et al. 2003; Taylor et al. 2009) and fluid shear (Lu et al. 2012; Turner and Pavalko 1998) in new bone formation. Skedros et al. (2003) have shown that sites experiencing shear strain had increased cortical thickness and lacunae density in turkey ulna mid-shaft, namely near the neutral axis. Srinivasan and Gross (2000) have also reported maximal fluid flow at these sites. Thus, shear strain may indirectly influ-

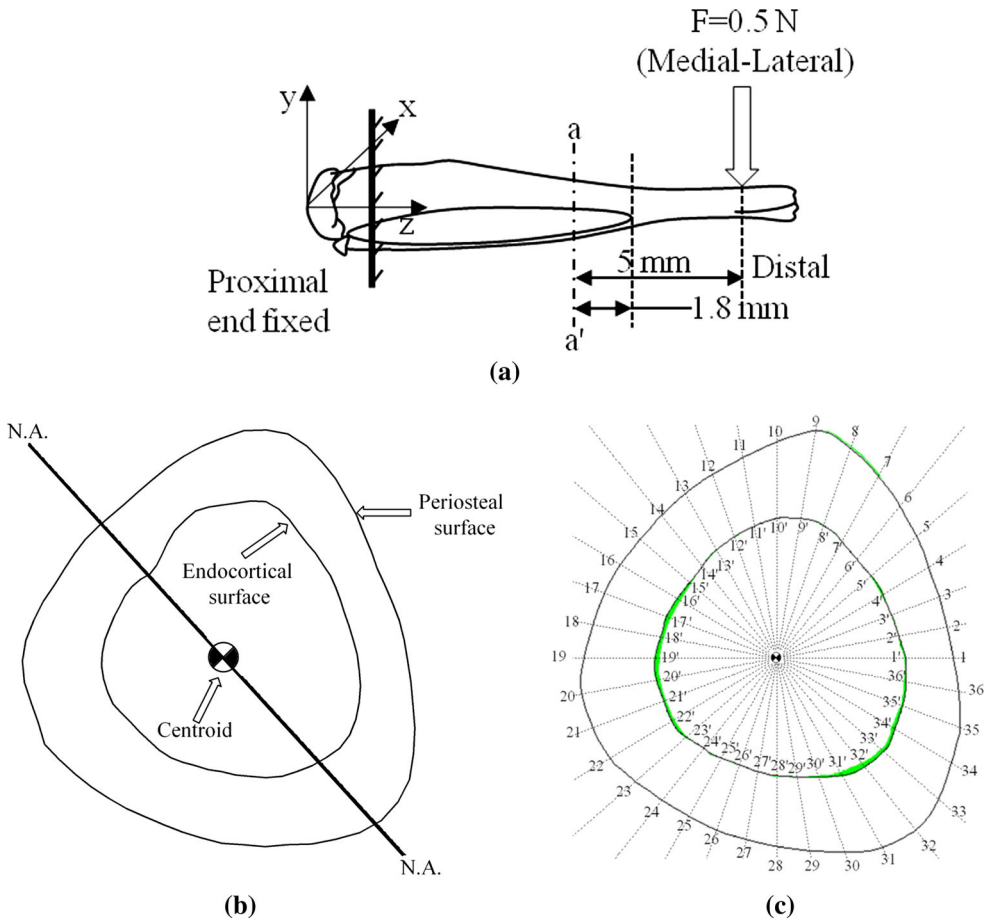

Fig. 1 **a** Loading configuration of murine tibia and **b** the idealized geometry of tibial cross section at section a–a′. The neutral axis (N.A.) is shown as a *solid straight line*. **c** Natural bone growth on control section (adapted from Fig. 3a of Srinivasan et al. 2002)

ence the fluid flow and thus the new bone formation. Carter et al. (1998) have also suggested that tissue level shear strain may induce distortional strain at cellular level and change cell shape. It disrupts the cell–extracellular matrix interaction and may initiate integrin-mediated bone remodelling activities (Marie 2013). Accordingly, osteogenesis as a function of shear strain versus as a function of fluid shear has been studied here, using a computational model based on algorithms proposed in previous studies (Cowin et al. 1985; Huiskes et al. 1987; Chennimalai Kumar et al. 2009). The model simulates loading-induced osteogenesis noticed in the in vivo study of Srinivasan et al. (2002). In the current approach, bone formation rate is assumed roughly proportional to strain energy densities (SED) due to primary as well as secondary stimuli in excess of their osteogenic thresholds. The osteogenic potentials of these stimuli are individually investigated. Subsequently, the effect of bending shear strain or fluid shear stress is combined with normal strain to predict osteogenesis. The combinations, viz. normal strain with shear strain and normal strain with fluid shear, predict results close to experimental values. This computational study may help to identify a simple and computationally easy relationship between site-specific osteogenesis and components of loading-induced mechanical environment, which may, in turn, prove useful in the development of therapeutic biomechanical interventions (such as physical exercises) for the prevention and treatment of bone loss.

2 Methods

2.1 Estimation of normal and shear strains

In the present study, we model osteogenesis for a case where tibia of a 10-week-old female C57Bl/6J mouse was subjected to a continuous cyclic cantilever loading of 0.5 N for 500 cycles at 1 Hz. This loading has been referred to as 'high-magnitude regimen' in Srinivasan et al. (2002). A mid-diaphyseal cross section located at 1.8 mm proximal to the tibia–fibula junction of the murine tibia has been idealized using 120 surface coordinates as shown in Fig. 1a, b. Geometric properties such as centroid, cortical area and area moment of inertia are estimated assuming the cross section is enclosed by linear piecewise curves. The neutral axis

Table 1 Values of the parameters used in the computer simulation

Parameters, symbol, units	Value
Young's modulus of the bone, E (GPA)	20[a]
Poisson's ratio of the bone, υ	0.3[b]
Shear modulus, $G\ (=E/(2(1+\upsilon)))$ (GPA)	7.69[a,b]
Young's modulus of the osteocyte, E_{osc} (kPa)	4.47[c]
Poisson's ratio of the osteocyte, υ_{osc}	0.3[c]
Shear modulus of the osteocyte, $G_{osc}\ (=E_{osc}/(2(1+\upsilon_{osc})))$ (kPa)	1.72[b,c]
Relative compressibility coefficient or Skempton pore pressure coefficient, B	0.53[d]
Diffusion coefficient, $c(\mathrm{m}^2/\mathrm{s})$	5.1×10^{-7}[e]
Poisson's ratio of the solid bone matrix under 'undrained conditions', υ_u	0.33[d]
Radius of canaliculus, $b_o(\mu\mathrm{m})$	0.2[d]
Radius of the cell process, $a_o(\mu\mathrm{m})$	0.1[d]
Local or small scale permeability constant, $k_p(\mathrm{m}^2)$	[d,h]4.49×10^{-18}
Surface remodelling rate coefficients, $C(\mathrm{unit}^4/\mathrm{timestep\text{-}Joule})$	$C_i^{\varepsilon_p}=C_i^{\varepsilon_c}=1\times10^{-8}$ $C_i^{\gamma_p}=C_i^{\gamma_c}=1\times10^{-6}$ $C_i^{s_p}=C_i^{s_c}=1$
Reference SED, $U_{ref}(\mathrm{Joule}/\mathrm{m}^3)$	$U_{ref}^{\varepsilon_p}=U_{ref}^{\varepsilon_c}=6400$[f,g] $U_{ref}^{\gamma_p}=U_{ref}^{\gamma_c}=195$[a] $U_{ref}^{\gamma_p}=U_{ref}^{\gamma_c}=$[c]$1\times10^{-4}$

[a] Prasad et al. (2010)
[b] Popov and Balan (1998)
[c] Verbruggen et al. (2012)
[d] Weinbaum et al. (1994)
[e] Cowin 1999
[f] Fritton et al. (2005)
[g] Srinivasan et al. (2007)
[h] Lemaire et al. (2012)

is assumed to be passing through the centroid. Its orientation has been adapted from the literature (Prasad et al. 2010; Srinivasan et al. 2013), where it was computed using finite element method (Fig. 1). Tibia is idealized as a linearly elastic, homogeneous, isotropic cantilever beam with Young's and shear moduli of 20 and 7.69 GPa, respectively, and is subjected to a load of 0.5 N at the free distal end (Fig. 1a). The loading waveform is taken similar to that given in Srinivasan et al. (2002). The beam theory was used to estimate normal and shear strains in the cortex, especially at periosteal and endocortical surfaces (Popov and Balan 1998):

$$\varepsilon_i = \frac{M\cdot y_i}{E\cdot I} \tag{1}$$

$$\gamma_i = \frac{V\cdot Q_i}{G\cdot I\cdot t_i} \tag{2}$$

where ε_i and γ_i are normal and shear strains, respectively, at any surface coordinate i (i = 1–120); M is the bending moment at the cross section; y_i is perpendicular distance between the surface coordinate and neutral axis; I is the second moment of area; V is the vertical shear force (0.5 N); Q_i is the first moment of the area lying above an axis passing through the point i and parallel to the neutral axis; t_i is the width of the section along an axis passing through point i and parallel to the neutral axis; E and G are Young's modulus and shear modulus, respectively (Table 1). The initial cortical area and area moment of inertia were 0.5042 mm^2 and 0.06 mm^4, respectively. Maximum normal strain calculated in the model was approximately 1311 με which is close to the in vivo strain values, i.e. 1330 ± 50 με.

2.2 Estimation of fluid shear

Osteocyte-level canalicular fluid flow parameters such as pore pressure and fluid shear stress induced due to bending has been estimated based on Weinbaum et al. (1994); Kameo et al. (2009), with an assumption that osteocytes are located close to surface coordinates and sense fluid shear to initiate osteoblastic activity on surfaces. Only steady-state response of fluid flow has been considered as the transient response attains steady state within a few seconds of loading (Srinivasan and Gross 2000).

The in vivo study considered here was subjected to a bending of trapezoidal waveform, which can be closely approximated as a Fourier series of sinusoidal waves (Srini-

vasan and Gross 2000). For numerical simplicity, a sinusoidal waveform is assumed. The periosteal and endocortical surfaces are assumed to be permeable to the fluid flow. The pore pressure due to a sinusoidal bending moment of frequency ω and amplitude M has been calculated as follows (Kameo et al. 2009):

$$P_{steady}(y^*, t) = \frac{BM(1+\upsilon_u)}{2a^2} \times \left\{ y^* \sin \Omega t^* - \mathrm{Im}\left[\left\{ \frac{\mathrm{i}\Omega H \sinh \sqrt{\mathrm{i}\Omega} y^* + 3y^*(\sinh \sqrt{\mathrm{i}\Omega} - \sqrt{\mathrm{i}\Omega} \cosh \sqrt{\mathrm{i}\Omega})}{\mathrm{i}\Omega H \sinh \sqrt{\mathrm{i}\Omega} + 3(\sinh \sqrt{\mathrm{i}\Omega} - \sqrt{\mathrm{i}\Omega} \cosh \sqrt{\mathrm{i}\Omega})} \right\} e^{\mathrm{i}\Omega t} \right] \right\} \quad (3)$$

where P_{steady} is the steady-state component of pore pressure induced due to bending; B is relative compressibility constant or Skempton coefficient; c is diffusion coefficient; M is the amplitude of bending moment; υ_u is Poisson's ratio of solid bone matrix under undrained conditions; i is the imaginary unit; a is the thickness of the cortex; y^*, Ω, t^* and H are non-dimensional parameters and are defined as:

$$y^* = \frac{y_i}{a}, \quad t^* = \frac{ct}{a^2}, \quad \Omega = \frac{a^2\omega}{c}, \quad H = \frac{1-\nu}{\nu_u - \nu}$$

where t is the time and ω is angular frequency of the applied load.

Fluid shear stress developed in canaliculi has been estimated based on the literature (Zeng et al. 1994; Weinbaum et al. 1994) as follows:

$$S_i = \frac{b_o}{\lambda} \frac{\partial P_{steady}}{\partial y^*} [A_1 I_1(\lambda/q) - B_1 K_1(\lambda/q)] \quad (4)$$

which implies

$$S_i = \frac{b_o}{\lambda} \frac{BM(1+\upsilon_u)}{2a^2} \times \left\{ \sin \Omega t^* - \mathrm{Im}\left[\left\{ \frac{\sqrt[3]{\mathrm{i}\Omega} H \cos \sqrt{\mathrm{i}\Omega} y^* + 3(\sinh \sqrt{\mathrm{i}\Omega} - \sqrt{\mathrm{i}\Omega} \cosh \sqrt{\mathrm{i}\Omega})}{\mathrm{i}\Omega H \sinh \sqrt{\mathrm{i}\Omega} + 3(\sinh \sqrt{\mathrm{i}\Omega} - \sqrt{\mathrm{i}\Omega} \cosh \sqrt{\mathrm{i}\Omega})} \right\} e^{i\Omega t} \right] \right\} \times [A_1 I_1(\lambda/q) - B_1 K_1(\lambda/q)] \quad (5)$$

where S_i is fluid shear stress at surface coordinate i; b_o is the radius of canaliculus; the resultant fluid flow or shear is oriented perpendicular to the neutral axis of bending towards direction 'y', i.e. directed from compression side to tensile side of the section; and

$$A_1 = \frac{K_O(\lambda) - K_O(\lambda/q)}{I_O(\lambda/q)K_O(\lambda) - I_O(\gamma)K_O(\lambda/q)} \quad (6)$$

$$B_1 = \frac{I_O(\lambda/q) - I_O(\lambda)}{I_O(\lambda/q)K_O(\lambda) - I_O(\lambda)K_O(\lambda/q)} \quad (7)$$

where K_o and I_o are the modified Bessel functions of the third and the first kind, respectively; q is a ratio of the radius of canaliculus (b_o) to the radius of cell process (a_o); $\lambda = b_o/\sqrt{k_p}$ is a dimensionless length ratio, where k_p is Darcy law permeability constant.

2.3 Computation of strain energy density (SED) and evolution of surface

The model computes normal and shear SED ($U_{\mathrm{i}}^{\varepsilon}$ and U_{i}^{γ}) along with the fluid shear SED (U_{i}^{s}) at periosteal and endocortical surfaces as follows:

$$U_i^{\varepsilon} = \frac{1}{2} E.\varepsilon_i^2 \quad (8)$$

$$U_i^{\gamma} = \frac{1}{2} G.\gamma_i^2 \quad (9)$$

$$U_i^{s} = \frac{S_i^2}{2G_{osc}} \quad (10)$$

where G_{osc} is the shear modulus of osteocyte. The model uses SED as a stimulus for new bone formation. In the literature (Fritton et al. 2005; Srinivasan et al. 2007; Weinbaum et al. 1994), normal strain of magnitude 800 $\mu\varepsilon$ and fluid shear of 6 dyne/cm^2 (0.6 Pa) are considered sufficient to initiate bone remodelling activities at cellular level. Accordingly, reference SEDs (U_{ref}) have been computed corresponding to these values of osteogenic thresholds of each stimulus and are listed in Table 1. The difference between estimated and reference SED is assumed to govern osteogenesis (Cowin 1993). The growth law is applied to simulate new bone formation and is similar to that proposed by Chennimalai Kumar et al. (2009):

$$\frac{\partial c_i}{\partial t} = \begin{cases} C(U_i - U_{ref}), & if\ U_i > U_{ref} \\ 0, & \text{otherwise} \end{cases} \quad (11)$$

where $\frac{\partial c_i}{\partial t}$ represents the bone formation rate and C is the bone's surface remodelling rate coefficient.

The following assumptions have been made based on Carter et al. (1998); Burr et al. (2002); Carpenter (2006); Carpenter and Carter (2008); Feldman et al. (2007):

- The osteogenic response may depend on the nature of normal strain (viz. compressive vs. tensile).
- The osteogenic response may be different for different components of mechanical milieu (viz. normal strain vs. shear strain vs. fluid flow-induced shear stress).
- The osteogenic response of periosteal and endocortical surfaces may differ from each other according to their mechano-biological environment as endocortical surface has been reported to be more mechano-responsive than periosteal surface due to additional recruitment of osteoblasts from bone marrow osteoprogenitors (Birkhold et al. 2016; Turner et al. 1998).

Based on the above assumptions, different thresholds were considered for different surfaces (periosteal vs. endocortical) and different components of mechanical environment (normal strain vs. shear strain vs. fluid shear stress). We have incorporated the natural growth in the model based on new bone distribution noticed in 0.25 N loading group (Fig. 1c) which has been treated as control due to unavailability of original control's site-specific data and similarity in bone formation rate to control group. The growth law is modified accordingly as follows:

Normal strain as the stimulus for periosteal and endocortical surfaces, respectively:

$$\frac{\partial c_i^{\varepsilon_p}}{\partial t} = \begin{cases} C_i^{\varepsilon_p}(U_i^{\varepsilon_p} - U_{ref}^{\varepsilon_p}) + \Delta_i, & if\ U_i^{\varepsilon_p} > U_{ref}^{\varepsilon_p} \\ \Delta_i, & \text{otherwise} \end{cases} \tag{12}$$

and

$$\frac{\partial c_i^{\varepsilon_c}}{\partial t} = \begin{cases} C_i^{\varepsilon_c}(U_i^{\varepsilon_c} - U_{ref}^{\varepsilon_c}) + \Delta_i, & if\ U_i^{\varepsilon_c} > U_{ref}^{\varepsilon_c} \\ \Delta_i, & \text{otherwise} \end{cases} \tag{13}$$

Shear strain as the stimulus for periosteal and endocortical surfaces, respectively:

$$\frac{\partial c_i^{\gamma_p}}{\partial t} = \begin{cases} C_i^{\gamma_p}(U_i^{\gamma_p} - U_{ref}^{\gamma_p}) + \Delta_i, & if\ U_i^{\gamma_p} > U_{ref}^{\gamma_p} \\ \Delta_i, & \text{otherwise} \end{cases} \tag{14}$$

and

$$\frac{\partial c_i^{\gamma_c}}{\partial t} = \begin{cases} C_i^{\gamma_c}(U_i^{\gamma_c} - U_{ref}^{\gamma_c}) + \Delta_i, & if\ U_i^{\gamma_c} > U_{ref}^{\gamma_c} \\ \Delta_i, & \text{otherwise} \end{cases} \tag{15}$$

Fluid shear stress as the stimulus for periosteal and endocortical surfaces, respectively:

$$\frac{\partial c_i^{s_p}}{\partial t} = \begin{cases} C_i^{s_p}(U_i^{s_p} - U_{ref}^{s_p}) + \Delta_i, & if\ U_i^{s_p} > U_{ref}^{s_p} \\ \Delta_i, & \text{otherwise} \end{cases} \tag{16}$$

and

$$\frac{\partial c_i^{s_c}}{\partial t} = \begin{cases} C_i^{s_c}(U_i^{s_c} - U_{ref}^{s_c}) + \Delta_i, & if\ U_i^{s_c} > U_{ref}^{s_c} \\ \Delta_i, & \text{otherwise} \end{cases} \tag{17}$$

where parameters with superscripts ε_p and ε_c correspond to normal strain at periosteal and endocortical surfaces, respectively; similarly, γ_p and γ_c represent shear strains, whereas s_p and s_c correspond to the fluid shear stress at the respective surfaces. Δ_i is the parameter representing natural growth rate at surface coordinate 'i', which is zero for the periosteal surface since growth is nearly absent in the referred in vivo study (Srinivasan et al. 2002), whereas for the endocortical surface, it has been estimated at each surface coordinate 'i' by dividing new bone thickness on control section (Fig. 1c) by total loading time period. A biologically consistent value of remodelling rate coefficient, C, has been calculated based on the mineral apposition rate (MAR) found from earlier in vivo studies by curve-fitting the corresponding bone growth law to the experimental results (Cowin et al. 1985; Srinivasan et al. 2002; Chennimalai Kumar et al. 2009). The baseline values of reference SED (U_{ref}) for different components and surfaces are decided based on osteogenic fluid shear and physiological strains (Weinbaum et al. 1994; Srinivasan et al. 2007; Prasad et al. 2010; Verbruggen et al. 2012), which are given in Table 1.

If at any instance, the SED (U_i) at surface coordinates 'i' reaches value above threshold, the coordinate shifts in the normal direction to the bone surface to incorporate osteogenesis. The model updates the geometry of the cross section according to the following time stepping scheme:

$$X_i\,(t + dt) = X_i\,(t) + \frac{\partial c_i}{\partial t} dt \cos\theta \tag{18}$$

$$Y_i\,(t + dt) = Y_i\,(t) + \frac{\partial c_i}{\partial t} dt \sin\theta \tag{19}$$

where $X_i(t + dt)$ and $Y_i(t + dt)$ are the new coordinates at time $t + dt$, while $X_i(t)$ and $Y_i(t)$ are the old coordinates at time t and dt is the time step size (increment). θ is the angle that the unit vector perpendicular to the surface at the point in consideration makes with X-direction. The algorithm used for the present study is shown in Fig. 2. The model uses a time step of 1 second and iterates for a total time period of 500 s, which corresponds to number of loading cycles.

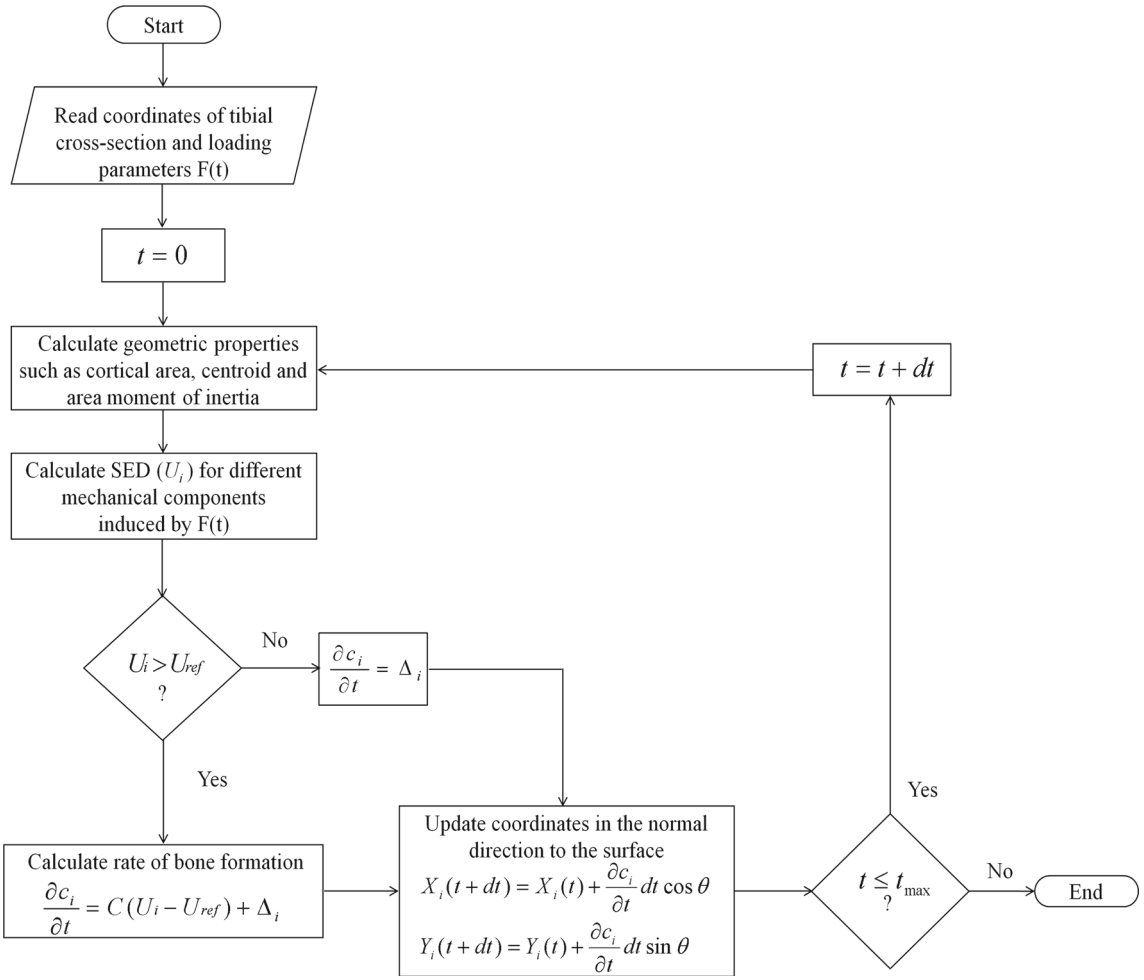

Fig. 2 Fundamental algorithm used for the simulation of osteogenesis

Table 2 Combinations of mechanical stimuli used to test the model

S. No.	Mechanical Stimuli
1	Normal strain (compressive and tensile)
2	Shear strain
3	Normal strain plus shear strain
4	Tensile normal strain plus shear strain
5	Interstitial fluid shear stress
6	Normal strain plus fluid shear stress

3 Results

The model simulates osteogenesis considering three different components of mechanical environment: normal strain, shear strain and fluid flow-induced shear stress, individually as well as in their combinations, viz. normal strain with shear strain or with fluid shear (Table 2). To measure site-specific osteogenesis, the circumference of the cross section is divided with 36 radial lines, each 10^{o} apart from the neighbouring lines and passing through the centroid of the cross section. These lines intersect periosteal and endocortical circumferences at the points numbered in counterclockwise direction as 1–36 at periosteal surface and as $1'$ to $36'$ at endocortical surface (see Fig. 3a). The new bone thickness thus measured has been compared with experimental new bone thickness obtained from histological cross section (Srinivasan et al. 2002, 0.5 N loading case), along these radial lines. Simulation results are described in the following subsections.

3.1 Normal strain

Osteogenic potential of normal strain has been investigated by considering (i) normal strains (i.e., compressive and tensile strain) alone to be osteogenic and (ii) only tensile normal strain to be osteogenic. When normal strain is considered, new bone is formed away from neutral axis, namely at periosteal points 1–10 and 17–27, out of which points 1–10 only have osteogenesis in accordance with the in vivo study (Fig. 3b). When only tensile normal strain is consid-

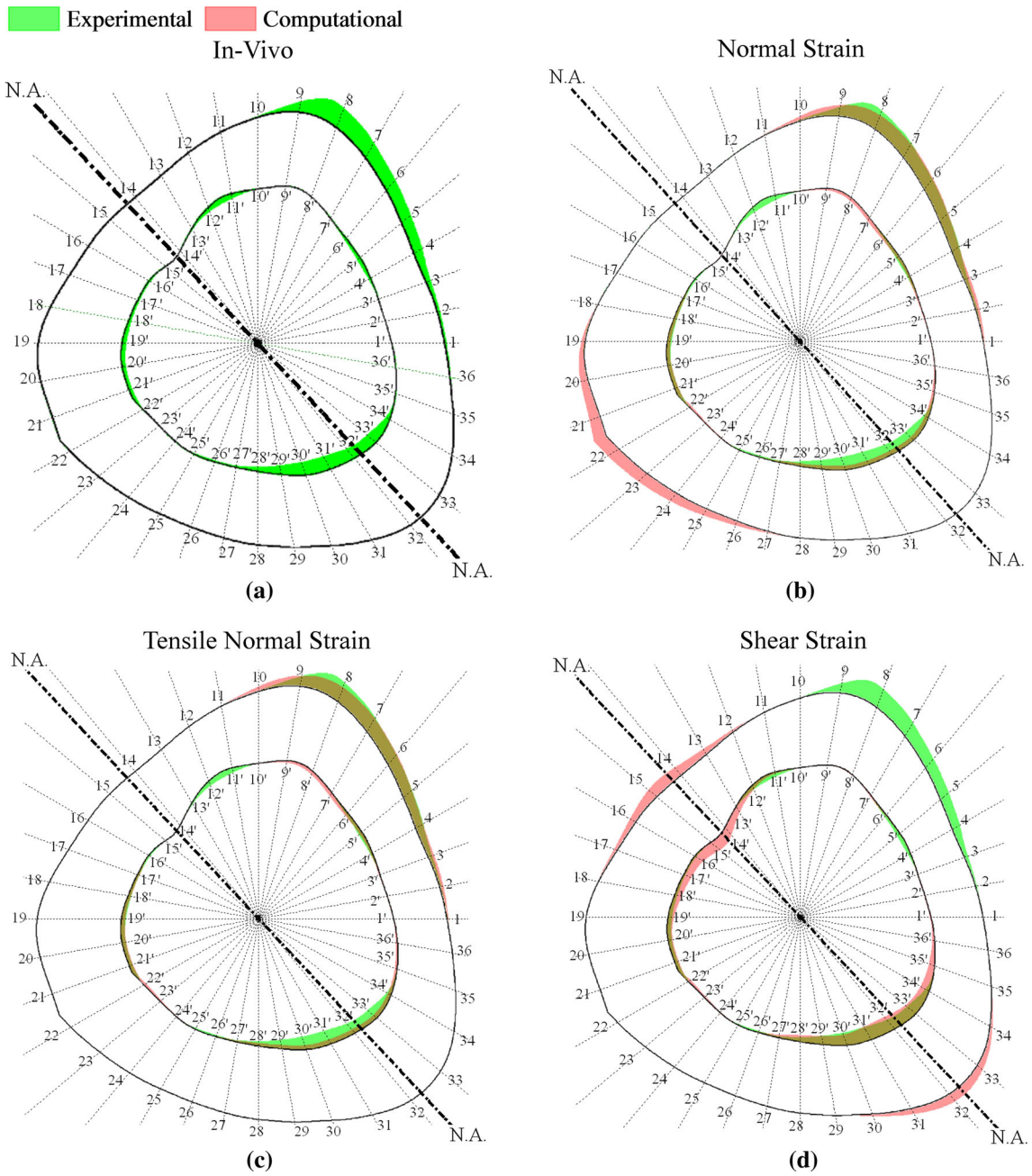

Fig. 3 Computational versus experimental results: **a** in vivo new bone formation (*green*) in murine tibia (adapted from Fig. 3b of Srinivasan et al. 2002); and computational prediction of osteogenesis (*red*) due to: **b** normal strain only, **c** tensile normal strain only and **d** shear strain only. The cross section has been divided into 36 sectors in order to compare site-specific osteogenesis. The overlap of experimental and computational osteogenesis is shown in *red-green* mixture

ered, the model predicts new bone formation away from the neutral axis along periosteal points 1–10 and endocortical points 3′–9′ and 16′–23′ similar to experimental observation (Fig. 3c), whereas it fails around the neutral axis along endocortical points 26′–35′ and 10′–14′ (Fig. 3c). If compressive normal strain were considered alone, new bone would be formed along posterior-medial sites in contrast with the experimental observation. The above findings confirm that normal strain may not be the sole stimulus for osteogenesis.

3.2 Shear strain

Shear strain as a sole stimulus in the model predicts new bone formation near the neutral axis along periosteal points 11–18 and 30–35, and endocortical points 10′–23′ and 27′–36′,

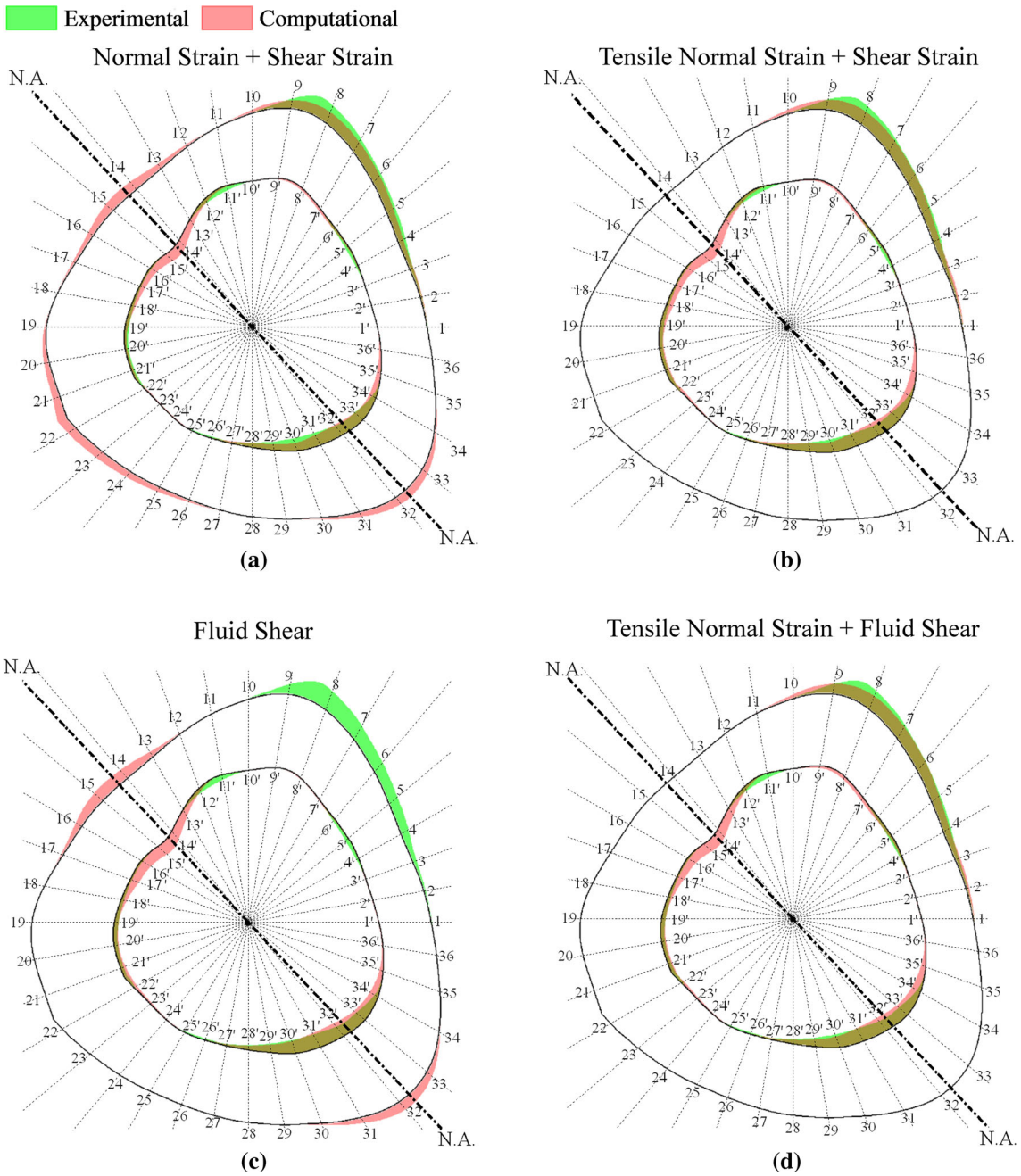

Fig. 4 Computational prediction of osteogenesis, when: **a** normal and shear strains are combined, **b** tensile normal strain and shear strain are combined, **c** fluid shear is considered alone, **d** fluid shear is considered along with tensile normal strain

among which points 27′–36′ and 19′–23′ only have new bone formed in the experimental study (Fig. 3d). Thus, shear strain as a stimulus fails to completely model osteogenesis.

3.3 Normal plus shear strain

When the effects of normal strains (both tensile and compressive) and solid shear strains are added, the site-specific new bone formation at endocortical surface was found close to experimental observation (Fig. 4a); however, the model falsely predicts osteogenesis at periosteal points 12–17, 19–26 and 29–35 (Fig. 4a). Thus, this combination also fails to accurately model osteogenesis.

3.4 Tensile normal strain plus shear strain

The results improve when tensile strain is considered in combination with shear strain with an assumption that endo-

cortical surface is more mechano-responsive as compared to periosteal surface (Carter et al. 1998; Carpenter 2006; Feldman et al. 2007; Birkhold et al. 2016) (Fig. 4b). The sites of new bone formation predicted by the model are close to that noticed during the in vivo study (Fig. 4b) except for only 5 endocortical sites 13′–17′ (out of total 36 points compared) where the model overestimates new bone formation.

3.5 Interstitial fluid shear stress

Canalicular fluid flows from compression to tension side when bones are subjected to mechanical loading (Turner and Pavalko 1998; Tate et al. 2000). In vitro studies on the bone cells (such as osteoblasts and osteocytes) have found that the fluid flow is a stimulus to osteogenic activities (Huo et al. 2008; Lu et al. 2012). Accordingly, when the interstitial fluid flow is considered osteogenic, the model predicts new bone formation near neutral axis along periosteal points 12-17 and 29-35 and endocortical points 10′-17′, 20′-23′ and 27′-35′, which is similar to that obtained due to solid shear strain (Fig. 4c). The model, however, fails to fit the experimental new bone distribution along the periosteal points 1–10 (Fig. 4c).

The model predicts the peak fluid velocity and shear stress as 18 μm/s and 10 dyne/cm^2 respectively, which are close to 20.37 μm/s and 18 dyne/cm^2, respectively, calculated from empirical relations reported in several in vivo studies (Price et al. 2011; Wang et al. 2013; Jing et al. 2014). The difference in fluid shear magnitude may be attributed to the difference in loading condition; nevertheless, it is in the range of shear stress required to induce calcium signaling and new bone formation (Weinbaum et al. 1994). Moreover, the model's prediction of maximal flow near minimal strain sites aligns with the findings of several in silico studies (Steck et al. 2000; Tate et al. 2000; Hamilton et al. 2004).

3.6 Normal strain plus interstitial fluid shear stress

Fluid flow-induced shear stress combined with tensile normal strain predicts site-specific new bone formation similar to the in vivo experiment (Fig. 4d). It may support the idea that (i) fluid shear acts as a secondary stimulus of osteogenic activity along with normal strain and (ii) different components of loading-induced mechanical environment may act collectively to adapt bone.

The experimental new bone thickness has been compared site-specifically with model's predictions for (i) tensile strain plus solid shear strain and (ii) tensile strain plus fluid shear stress in Fig. 5. The three cases have approximately similar new bone distribution, except for a few endocortical points. The computational model predicts an overall increase in cortical area approximately by 6.7 % (from 0.5042 to 0.538 mm^2) for the above two cases, which is close to that of 4.75 % found during the in vivo study. The error between computational and experimental new bone thickness shows that the model only underestimates or overestimates the new bone formation at periosteal points 10–11 and endocortical points 12′-16′, respectively (Fig. 5c, d). The osteogenic potentials of shear strain and fluid flow-induced shear strain are also site-specifically compared at periosteal and endocortical surfaces (Fig. 6a, b). Both showed similar site-specific osteogenic response in terms of new bone thickness.

4 Discussion and conclusions

This study suggests that shear strain or fluid shear stress may be responsible for osteogenesis near the sites of minimal normal strain; however, two or more stimuli (e.g., normal strain with shear strain or fluid shear) may be required to accurately model osteogenesis. This is in contrast to most of the previous in silico studies (Martínez and Cerrolaza 2006; Chennimalai Kumar et al. 2010), where a single stimulus such as normal strain energy density was typically used. These models had limitations to fit those experiments where new bone formation was present near minimal strain sites. The current study fills this gap. The comparison of shear strain and fluid shear stress in terms of new bone thickness suggests that they are equivalent in terms of their osteogenic potentials. Studies done by Skedros et al. (2003); Srinivasan and Gross (2000) also confirm the same. It provides a new perspective that macro-level shear strain can be used to estimate osteogenic potential of micro-level fluid shear, thus reducing computational and analytical complexities of the bone remodelling models. For example, Fig. 7 shows new bone distribution on tibial cross section (adapted from various in vivo studies) corresponding to different loading conditions. In all cases, osteogenesis can be seen away from as well as near the neutral axis, which may be modelled incorporating normal as well as shear components of mechanical environment. The present model would be helpful to model such experiments; however, it may fail in case of four-point bending, as there is no solid shear strain and new bone formation is still present around the neutral axis at periosteal surface. Incorporation of fluid flow may be required in that case to closely model osteogenesis. Moreover, as the loading frequency, number of cycles, time period and rest-inserted loading also affect the fluid flow and hence osteogenesis (Pereira et al. 2015; Malachanne et al. 2011), consideration of fluid flow in addition to mechanical components may improve the computational model (Pereira and Shefelbine 2014). Past research efforts have shown that different mechanical stimuli may opt different mechanisms of mechano-transduction to initiate remodelling activity at cellular level. For example, normal strain can be directly sensed by mechano-receptors located at osteoblast cell membrane

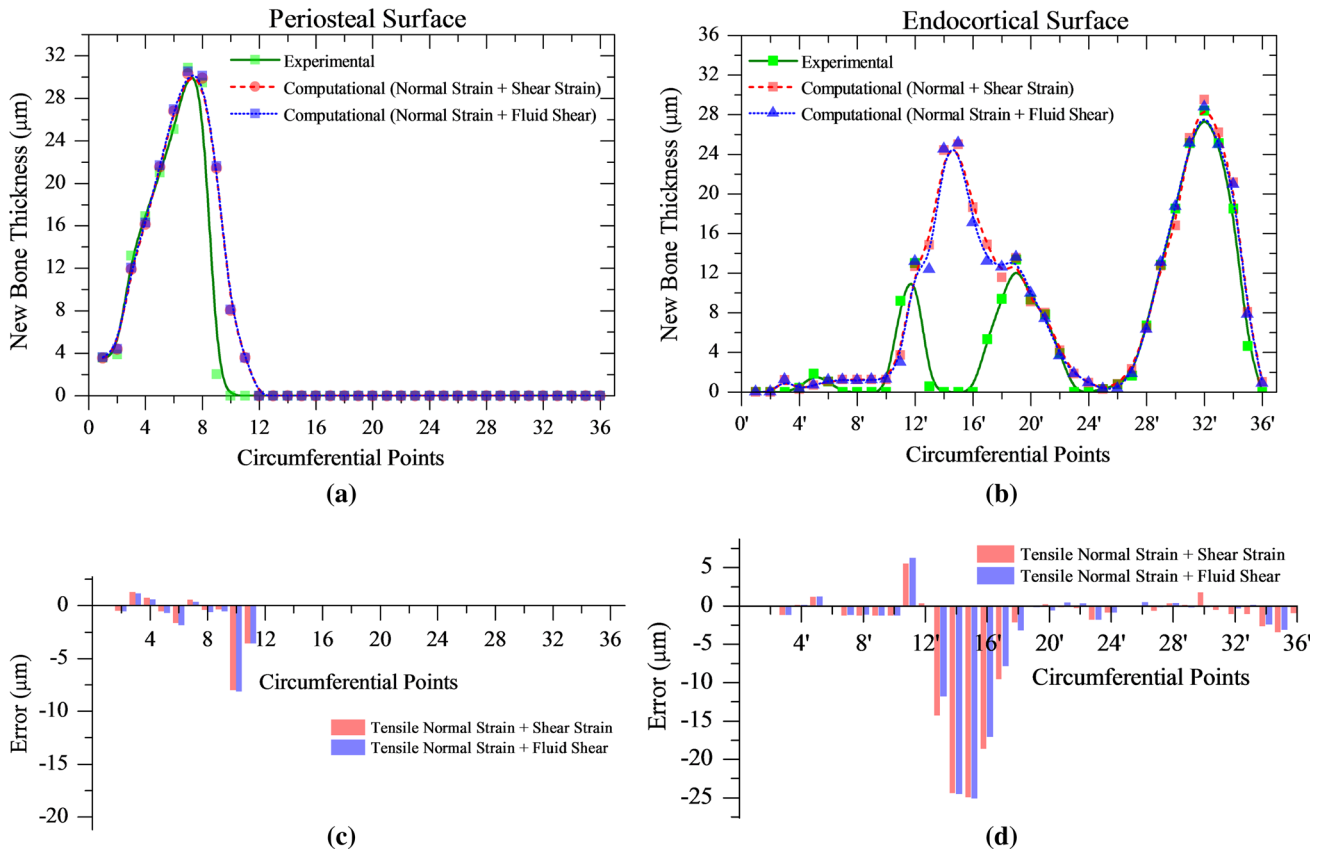

Fig. 5 Experimental versus computational new bone thickness when the tensile normal strain is considered along with the shear strain or the fluid shear at: **a** periosteal and **b** endocortical surfaces. The error (experimental–computational) in new bone thickness is shown at: **c** periosteal and **d** endocortical surfaces

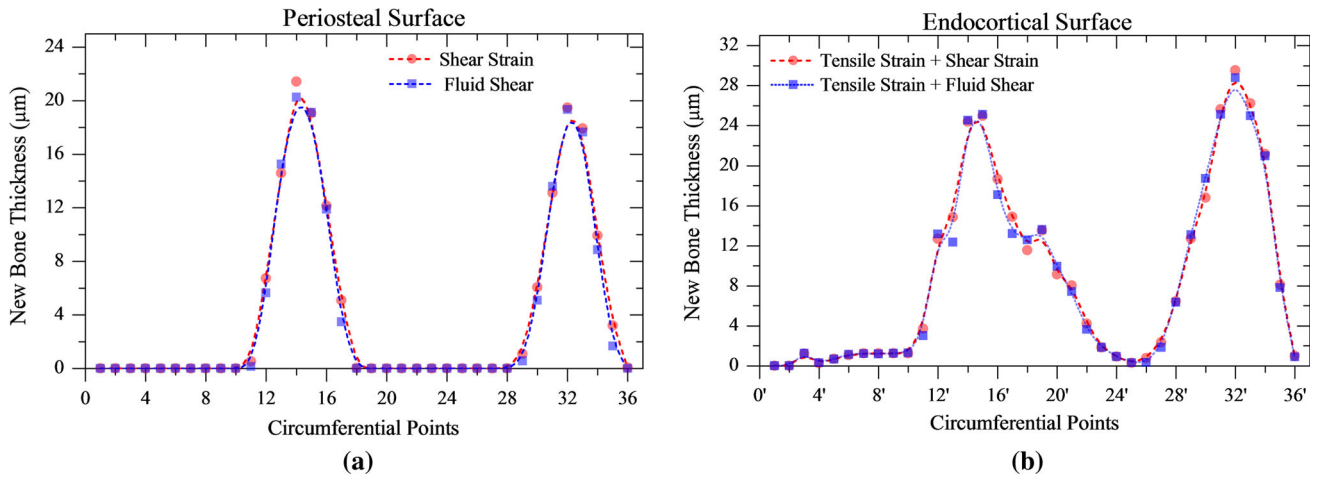

Fig. 6 Computationally obtained new bone thickness due to the shear strain as compared to that due to the fluid shear at: **a** periosteal and **b** endocortical surfaces

which may increase the calcium signaling and in turn the new bone formation. Strain also restructures the cytoskeleton of bone cell to regulate bone remodelling activities. In addition, tissue deformation/strain allows the interstitial fluid to flow through the osteocyte network. This fluid flow imparts shear stress on cell membrane of osteocytes which releases different signaling molecules such as prostaglandin (PGE_2) and NO in order to communicate with osteoblasts to initiate new bone formation (Turner and Pavalko 1998). Thus, incorporation of normal strain and fluid flow in the model may be useful in capturing the characteristics of cellular modelling activities.

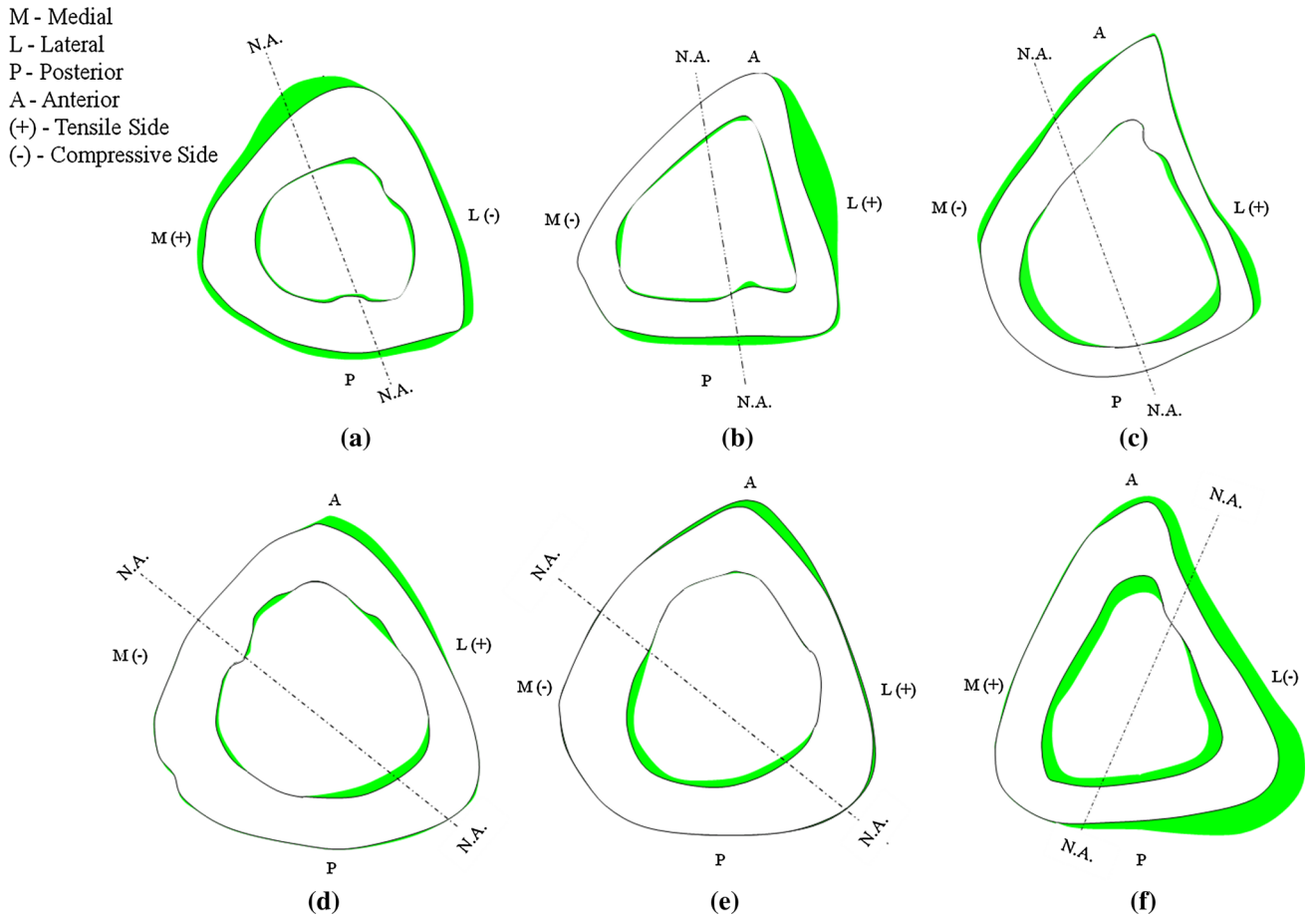

Fig. 7 Schematic representation of the new bone formation noticed during in vivo studies in response to different loading conditions such as **a** four-point bending (adapted from Roberts et al. 2009); **b** three-point bending (adapted from Sakai et al. 2011); **c** three-point bending (adapted from Matsumoto et al. 2008); **d** cantilever bending (adapted from Srinivasan et al. 2002); **e** cantilever bending (adapted from LaMothe 2004); **f** axial compression (adapted from Sugiyama et al. 2010)

The model predicts osteogenesis also at those sites where mechanical integrity is least challenged, e.g. around the neutral axis. Previous studies have explained that asymmetric bone morphology allows the bone to be bent in a predictable direction, i.e. about the neutral axis of bending during locomotion, and thus bone sacrifices its strength for predictable strain environment (Bertram and Biewener 1988). It permits the bone to adjust its morphology against any long-lasting stimulus (Main 2007). The new bone addition near neutral axis will not affect overall strain distribution; rather, it will fortify the environment to ensure that bones are loaded in a predictable fashion (Judex et al. 1997). This can be considered as a compromise between maintaining optimum strain level while ensuring that bone upholds a sufficient safety factor to withstand atypical loading (Wallace et al. 2014). Osteogenesis may, thus, have potential to align with the bone 's neutral axis. This aspect was ignored in previous models.

A few in vivo studies noticed that peak circumferential strain gradient (an indirect measure of maximal fluid flow) closely correlates with new bone formation near the neutral axis (Gross et al. 1997; Judex et al. 1997). In the present study, maximum osteogenic response due to fluid flow has indeed been observed near the neutral axis and thus the model's findings are in agreement with aforementioned studies. These findings may be useful in designing weight-bearing exercises where induced neutral axis will align with the sites requiring enhanced structural strength.

It has been noticed that fluid shear stress on osteocytic cell processes and fluid drag force on pericellular matrix fibres (i.e. tethering elements between cell transmembrane proteins and proteins in the extracellular matrix which accommodate the space between the cell body and the lacunae wall) both can potentially induce new bone formation (Pereira et al. 2015). Based on some previous work (You et al. 2001), however, canalicular fluid shear stress/force may be assumed to be proportional to pericellular drag force and flow velocity. The canalicular fluid stress has therefore been solely considered in the present model.

One limitation of this study is that only one histological cross section from a single animal has been used as a baseline to be compared with model output. As individual animals may have slightly different bone geometry and osteogenic, biological environment, there may be difference in site-specific new bone formation. The robustness of the model may, therefore, be improved by incorporating data from a group of animals, rather than a single animal currently used. Nevertheless, the baseline histological cross section used for the current model represents a typical new bone distribution near minimal strain sites/neutral axis observed in other in vivo studies where tibia of C57Bl/6J mice of different age groups was given cantilever bending (LaMothe et al. 2004; Srinivasan et al. 2003; Srinivasan et al. 2010; and Srinivasan et al. 2002). In addition, the presence of new bone formation near the minimal strain sites/neutral axis has been observed in several other in vivo studies (Wallace et al. 2014; Judex et al. 1997; Gross et al. 1997; Mosley et al. 1997). The model's accuracy may also be tested in future to predict osteogenesis at different sites along tibial length as these sites will experience different strain patterns.

The model does not incorporate possible bone resorption at several locations which might have been occurred as a result of, for example, damage imparted by high-magnitude strain. The model assumes that osteocytes positioned in the vicinity of tibial surfaces receive and integrate the signals from the other osteocytes in the network and communicate with lining cells/surface osteoblasts to initiate remodelling activity. Thus, the local effect of the fluid flow has been considered in the model (Pereira et al. 2015) although the flow should ideally be estimated across the osteocyte network. The model overlooks this effect not only to make the simulation computationally easy but also to remain consistent with other stimuli such as normal and shear strains, which have been considered at the endocortical and periosteal surfaces only. Incorporation of network's effect has been taken as a future work. Moreover, signaling molecules such as prostaglandins (PGE_2), nitric oxide (NO), sclerostin and ATP diffuse through extracellular fluid and communicate with neighbouring osteoblasts/osteocytes and, thus, are considered as potential regulators of new bone formation (Robling et al. 2006; Lu et al. 2012; Klein-Nulend et al. 2012). This paracrine mechanism has not been considered in the current model to reduce complexity and has, however, been taken as a future work.

Acknowledgements The authors acknowledge the institute fellowship and the computational facilities provided by IIT, Ropar, for this study.

Compliance with ethical standards

Conflicts of interest The authors declare that they do not have any conflict of interest.

References

Akhter MP, Raab DM, Turner CH, Kimmel DB, Recker RR (1992) Characterization of in vivo strain in the rat tibia during external application of a four-point bending load. J Biomech 25:1241–1246. doi:10.1016/0021-9290(92)90082-C

Ausk BJ, Gross TS, Srinivasan S (2006) An agent based model for real-time signaling induced in osteocytic networks by mechanical stimuli. J Biomech 39:2638–2646. doi:10.1016/j.jbiomech.2005.08.023

Beamer WG, Donahue LR, Rosen CJ, Baylink DJ (1996) Genetic variability in adult bone density among inbred strains of mice. Bone 18:397–403. doi:10.1016/8756-3282(96)00047-6

Bertram JE, Biewener AA (1988) Bone curvature: sacrificing strength for load predictability? J Theor Biol 131:75–92

Birkhold AI, Razi H, Duda GN, Weinkamer R, Checa S, Willie BM (2014) Mineralizing surface is the main target of mechanical stimulation independent of age: 3D dynamic in vivo morphometry. Bone 66:15–25. doi:10.1016/j.bone.2014.05.013

Birkhold AI, Razi H, Duda GN, Weinkamer R, Checa S, Willie BM (2016) The Periosteal Bone Surface is Less Mechano-Responsive than the Endocortical. Sci Rep 6:1–11

Brown TD, Pedersen DR, Gray ML et al (1990) Toward an identification of mechanical parameters initiating periosteal remodeling: A combined experimental and analytic approach. J Biomech 23:893–905. doi:10.1016/0021-9290(90)90354-6

Burr DB, Robling AG, Turner CH (2002) Effects of biomechanical stress on bones in animals. Bone 30:781–786. doi:10.1016/S8756-3282(02)00707-X

Carpenter RD (2006) Mechanobiology of bone cross-sectional development, adaptation, and strength. Dissertation, Stanford University

Carpenter RD, Carter DR (2008) The mechanobiological effects of periosteal surface loads. Biomech Model Mechanobiol 7:227–242. doi:10.1007/s10237-007-0087-9

Carter RD, Beaupré GS, Giori NJ, Helms JA (1998) Mechanobiology of skeletal regeneration. Clin Orthop 355:S41–S55

Chennimalai Kumar N, Dantzig JA, Jasiuk IM et al (2009) Numerical modeling of long bone adaptation due to mechanical loading: Correlation with experiments. Ann Biomed Eng 38:594–604. doi:10.1007/s10439-009-9861-4

Cowin SC (1993) Bone stress adaptation models. J Biomech Eng 115:528–533. doi:10.1115/1.2895535

Cowin SC, Hart RT, Balser JR, Kohn DH (1985) Functional adaptation in long bones: establishing in vivo values for surface remodeling rate coefficients. J Biomech 18:665–684

De Souza RL, Matsuura M, Eckstein F et al (2005) Non-invasive axial loading of mouse tibiae increases cortical bone formation and modifies trabecular organization: A new model to study cortical and cancellous compartments in a single loaded element. Bone 37:810–818. doi:10.1016/j.bone.2005.07.022

De Margerie E, Sanchez S, Cubo J, Castanet J (2005) Torsional resistance as a principal component of the structural design of long bones: comparative multivariate evidence in birds. Anat. Rec A Discov Mol Cell Evol Biol 282:49–66

Dirschl DR, Henderson RC, Oakley WC (1997) Accelerated bone mineral loss following a hip fracture: a prospective longitudinal study. Bone 21:79–82. doi:10.1016/S8756-3282(97)00082-3

Feldman D, Marcus R, Nelson D, Rosen CJ (2007) Chapter 21—Skeletal development: mechanical consequences of growth, aging, and disease. In: Marcus R, Feldman D, Nelson DA, Rosen CJ (eds) Osteoporosis. Elsevier Science, New York, pp 563–600

Ferguson VL, Ayers RA, Bateman TA, Simske SJ (2003) Bone development and age-related bone loss in male C57BL/6J mice. Bone 33:387–398. doi:10.1016/S8756-3282(03)00199-6

Florio CS, Narh KA (2012) Effect of modeling method on prediction of cortical bone strength adaptation under various loading conditions. Meccanica 48:393–413. doi:10.1007/s11012-012-9609-3

Flurkey K, Currer J, Harrison D (2007) Chapter 20—Mouse models in aging research. In: James GF, Barthold S, Davisson M, Newcomer CE, Quimby FW, Smith A (eds) The mouse in biomedical research, Second edn. Academic Press, Burlington, pp 637–672

Fridez P, Rakotomanana L, Terrier A, Leyvraz P (1998) Three dimensional model of bone external adaptation. In: Middleton J, Jones M, Pande G (eds) Computer Methods In Biomechanics & Biomedical Engineering 2: 189–196

Fritton J, Myers E, Wright T, Vandermeulen M (2005) Loading induces site-specific increases in mineral content assessed by microcomputed tomography of the mouse tibia. Bone 36:1030–1038. doi:10.1016/j.bone.2005.02.013

Gross TS, Edwards JL, Mcleod KJ, Rubin CT (1997) Strain gradients correlate with sites of periosteal bone formation. J Bone Miner Res 12:982–988. doi:10.1359/jbmr.1997.12.6.982

Hamilton N, Coombe D, Tran D, Zernicke RF (2004) Simulating load induced fluid flow and nutrient transport in bone. 5th Comb. Meet. Orthop. Res. Soc. Can. USA Jpn. Eur

Hillam RA, Skerry TM (1995) Inhibition of bone resorption and stimulation of formation by mechanical loading of the modeling rat ulna in vivo. J Bone Miner Res 10:683–689. doi:10.1002/jbmr.5650100503

Huiskes R, Weinans H, Grootenboer HJ et al (1987) Adaptive bone-remodeling theory applied to prosthetic-design analysis. J Biomech 20:1135–1150. doi:10.1016/0021-9290(87)90030-3

Huo B, Lu XL, Hung CT et al (2008) Fluid flow induced calcium response in bone cell network. Cell Mol Bioeng 1:58–66. doi:10.1007/s12195-008-0011-0

Inman CL, Warren GL, Hogan HA, Bloomfield SA (1999) Mechanical loading attenuates bone loss due to immobilization and calcium deficiency. J Appl Physiol 87:189–195

Jing D, Baik AD, Lu XL et al (2014) In situ intracellular calcium oscillations in osteocytes in intact mouse long bones under dynamic mechanical loading. FASEB J 28:1582–1592. doi:10.1096/fj.13-237578

Judex S, Gross TS, Zernicke RF (1997) Strain gradients correlate with sites of exercise-induced bone-forming surfaces in the adult skeleton. J Bone Miner Res 12:1737–1745. doi:10.1359/jbmr.1997.12.10.1737

Kameo Y, Adachi T, Hojo M (2009) Fluid pressure response in poroelastic materials subjected to cyclic loading. J Mech Phys Solids 57:1815–1827. doi:10.1016/j.jmps.2009.08.002

Kotha SP, Hsieh Y-F, Strigel RM et al (2004) Experimental and finite element analysis of the rat ulnar loading model—correlations between strain and bone formation following fatigue loading. J Biomech 37:541–548. doi:10.1016/j.jbiomech.2003.08.009

Klein-Nulend J, Bacabac R, Bakker A et al (2012) Mechanical loading and how it affects bone cells: the role of the osteocyte cytoskeleton in maintaining our skeleton. Eur Cell Mater 24:278–291

Kuruvilla SJ, Fox SD, Cullen DM, Akhter MP (2008) Site specific bone adaptation response to mechanical loading. J Musculoskelet Neuronal Interact 8:71–78

LaMothe JM (2004) Rest insertion combined with high-frequency loading enhances osteogenesis. J Appl Physiol 96:1788–1793. doi:10.1152/japplphysiol.01145.2003

Lau RY, Guo X (2011) A review on current osteoporosis research: with special focus on disuse bone loss. J Osteoporos 2011:1–6. doi:10.4061/2011/293808

Lee KCL, Maxwell A, Lanyon LE (2002) Validation of a technique for studying functional adaptation of the mouse ulna in response to mechanical loading. Bone 31:407–412. doi:10.1016/S8756-3282(02)00842-6

Lemaire T, Lemonnier S, Naili S (2012) On the paradoxical determinations of the lacuno-canalicular permeability of bone. Biomech Model Mechanobiol 11:933–946. doi:10.1007/s10237-011-0363-6

Levenston ME, Beaupré GS, Carter DR (1998) Loading mode interactions in simulations of long bone cross-sectional adaptation. Comput Methods Biomech Biomed Engin 1:303–319. doi:10.1080/01495739808936709

Lu XL, Huo B, Park M, Guo XE (2012) Calcium response in osteocytic networks under steady and oscillatory fluid flow. Bone 51:466–473. doi:10.1016/j.bone.2012.05.021

Lynch ME, Main RP, Xu Q et al (2011) Tibial compression is anabolic in the adult mouse skeleton despite reduced responsiveness with aging. Bone 49:439–446. doi:10.1016/j.bone.2011.05.017

Maimoun L, Fattal C, Micallef JP et al (2006) Bone loss in spinal cord-injured patients: from physiopathology to therapy. Spinal Cord 44:203–210. doi:10.1038/sj.sc.3101832

Main RP, Lynch ME, van der Meulen MCH (2010) In vivo tibial stiffness is maintained by whole bone morphology and cross-sectional geometry in growing female mice. J Biomech 43:2689–2694. doi:10.1016/j.jbiomech.2010.06.019

Main RP (2007) Ontogenetic relationships between in vivo strain environment, bone histomorphometry and growth in the goat radius. J Anat 210:272–293

Malachanne E, Dureisseix D, Jourdan F (2011) Numerical model of bone remodeling sensitive to loading frequency through a poroelastic behavior and internal fluid movements. J Mech Behav Biomed Mater 4:849–857

Marie PJ (2013) Targeting integrins to promote bone formation and repair. Nat Rev Endocrinol 9:288–295

Martínez G, Cerrolaza M (2006) A bone adaptation integrated approach using BEM. Eng Anal Bound Elem 30:107–115. doi:10.1016/j.enganabound.2005.08.010

Matsumoto HN, Koyama Y, Takakuda K (2008) Effect of mechanical loading timeline on periosteal bone formation. J Biomech Sci Eng 3:176–187. doi:10.1299/jbse.3.176

Mosley JR, March BM, Lynch J, Lanyon LE (1997) Strain magnitude related changes in whole bone architecture in growing rats. Bone 20:191–198

Moustafa A, Sugiyama T, Prasad J et al (2012) Mechanical loading-related changes in osteocyte sclerostin expression in mice are more closely associated with the subsequent osteogenic response than the peak strains engendered. Osteoporos Int 23:1225–1234. doi:10.1007/s00198-011-1656-4

Patel TK, Brodt MD, Silva MJ (2014) Experimental and finite element analysis of strains induced by axial tibial compression in young-adult and old female C57Bl/6 mice. J Biomech 47:451–457. doi:10.1016/j.jbiomech.2013.10.052

Pereira AF, Shefelbine SJ (2014) The influence of load repetition in bone mechanotransduction using poroelastic finite-element models: the impact of permeability. Biomech Model Mechanobiol 13:215–225. doi:10.1007/s10237-013-0498-8

Pereira AF, Javaheri B, Pitsillides A, Shefelbine S (2015) Predicting cortical bone adaptation to axial loading in the mouse tibia. PeerJ Prepr 3:e1390

Popov EP, Balan TA (1998) Engineering mechanics of solids, 2nd edn. Prentice Hall, Upper Saddle River

Prasad J, Wiater BP, Nork SE et al (2010) Characterizing gait induced normal strains in a murine tibia cortical bone defect model. J Biomech 43:2765–2770. doi:10.1016/j.jbiomech.2010.06.030

Price C, Zhou X, Li W, Wang L (2011) Real-time measurement of solute transport within the lacunar-canalicular system of mechanically loaded bone: Direct evidence for load-induced fluid flow. J Bone Miner Res 26:277–285. doi:10.1002/jbmr.211

Razi H, Birkhold AI, Zaslansky P et al (2015) Skeletal maturity leads to a reduction in the strain magnitudes induced within the bone:

a murine tibia study. Acta Biomater 13:301–310. doi:10.1016/j.actbio.2014.11.021

Roberts MD, Santner TJ, Hart RT (2009) Local bone formation due to combined mechanical loading and intermittent hPTH-(1–34) treatment and its correlation to mechanical signal distributions. J Biomech 42:2431–2438. doi:10.1016/j.jbiomech.2009.08.030

Robling AG, Castillo AB, Turner CH (2006) Biomechanical and molecular regulation of bone remodeling. Annu Rev Biomed Eng 8:455–498

Rubin CT, Recker R, Cullen D et al (2003) Prevention of postmenopausal bone loss by a low-magnitude, high-frequency mechanical stimuli: a clinical trial assessing compliance, efficacy, and safety. J Bone Miner Res 19:343–351. doi:10.1359/JBMR.0301251

Rubin CT, Lanyon LE (1985) Regulation of bone mass by mechanical strain magnitude. Calcif Tissue Int 37:411–417. doi:10.1007/BF02553711

Sakai D, Kii I, Nakagawa K et al (2011) Remodeling of actin cytoskeleton in mouse periosteal cells under mechanical loading induces periosteal cell proliferation during bone formation. PLoS ONE 6:e24847. doi:10.1371/journal.pone.0024847

Sample SJ, Collins RJ, Wilson AP et al (2010) Systemic effects of ulna loading in male rats during functional adaptation. J Bone Miner Res 25:2016–2028. doi:10.1002/jbmr.101

Shackelford LC (2004) Resistance exercise as a countermeasure to disuse-induced bone loss. J Appl Physiol 97:119–129. doi:10.1152/japplphysiol.00741.2003

Sheng M-C, Baylink DJ, Beamer WG et al (1999) Histomorphometric studies show that bone formation and bone mineral apposition rates are greater in C3H/HeJ (high-density) than C57Bl/6J (low-density) mice during growth. Bone 25:421–429

Skedros JG, Hunt KJ, Hughes PE, Winet H (2003) Ontogenetic and regional morphologic variations in the turkey ulna diaphysis: Implications for functional adaptation of cortical bone. Anat Rec A Discov Mol Cell Evol Biol 273:609–629

Somerville JM, Aspden RM, Armour KE et al (2004) Growth of C57bl/6 mice and the material and mechanical properties of cortical bone from the tibia. Calcif Tissue Int 74:469–475. doi:10.1007/s00223-003-0101-x

Srinivasan S (2003) Enabling bone formation in the aged skeleton via rest-inserted mechanical loading. Bone 33:946–955. doi:10.1016/S8756-3282(03)00274-6

Srinivasan S, Ausk BJ, Poliachik SL et al (2007) Rest-inserted loading rapidly amplifies the response of bone to small increases in strain and load cycles. J Appl Physiol 102:1945–1952. doi:10.1152/japplphysiol.00507.2006

Srinivasan S, Ausk BJ, Prasad J et al (2010) Rescuing loading induced bone formation at senescence. PLoS Comput Biol 6:e1000924. doi:10.1371/journal.pcbi.1000924

Srinivasan S, Gross TS (1999) Canalicular fluid flow in bone: A basis for bone formation at sites of minimal strain. 45th Ann Meet, Orthop. Res. Soc. ORS Poster

Srinivasan S, Gross TS (2000) Canalicular fluid flow induced by bending of a long bone. Med Eng Phys 22:127–133. doi:10.1016/S1350-4533(00)00021-7

Srinivasan S, Prasad J, Ausk BJ, Kwon R, Worton L, Gross TS, BainSD, Gardiner EM (2013) Concurrent optimization of Cyclosporin A and mechanical loading identifies multiple optima to rescue senescentbone adaptation. Orthop Res Soc ORS Poster

Srinivasan S, Weimer DA, Agans SC et al (2002) Low-magnitude mechanical loading becomes osteogenic when rest is inserted between each load cycle. J Bone Miner Res 17:1613–1620. doi:10.1359/jbmr.2002.17.9.1613

Steck R, Niederer P, Tate MK (2000) A finite difference model of load-induced fluid displacements within bone under mechanical loading. Med Eng Phys 22:117–125. doi:10.1016/S1350-4533(00)00017-5

Sugiyama T, Price JS, Lanyon LE (2010) Functional adaptation to mechanical loading in both cortical and cancellous bone is controlled locally and is confined to the loaded bones. Bone 46:314–321

Tate MK, Steck R, Forwood MR, Niederer P (2000) In vivo demonstration of load-induced fluid flow in the rat tibia and its potential implications for processes associated with functional adaptation. J Exp Biol 203:2737–2745

Taylor WR, Warner MD, Clift SE (2003) Finite element prediction of endosteal and periosteal bone remodelling in the turkey ulna: effect of remodelling signal and dead-zone definition. Proc Inst Mech Eng 217:349–356. doi:10.1243/095441103770802513

Taylor R, Zheng C, Jackson R, Doll J, Chen J, Holzbaur K, Besier T, Kuhl E (2009) The phenomenon of twisted growth: humeral torsion in dominant arms of high performance tennis players. Comput Methods Biomech Biomed Engin 12:83–93

Thompson DW (1942) On growth and form. In: Bonner JT (ed) Cambridge University, pp. 241

Turner CH, Forwood M, Rho JY, Yoshikawa T (1994) Mechanical strain threshold for lamellar bone formation. J Bone Miner Res 9:87–97

Turner CH, Pavalko FM (1998) Mechanotransduction and functional response of the skeleton to physical stress: the mechanisms and mechanics of bone adaptation. J Orthop Sci 3:346–355. doi:10.1007/s007760050064

Turner CH, Owan I, Alvey T, Hulman J, Hock J (1998) Recruitment and proliferative responses of osteoblasts after mechanical loading in vivo determined using sustained-release bromodeoxyuridine. Bone 22:463–469

Verbruggen SW, Vaughan TJ, McNamara LM (2012) Strain amplification in bone mechanobiology: a computational investigation of the in vivo mechanics of osteocytes. J R Soc Interface 9:2735–2744. doi:10.1098/rsif.2012.0286

Vico L, Collet P, Guignandon A et al (2000) Effects of long-term microgravity exposure on cancellous and cortical weight-bearing bones of cosmonauts. The Lancet 355:1607–1611. doi:10.1016/S0140-6736(00)02217-0

Wagner DW, Chan S, Castillo AB, Beaupre GS (2013) Geometric mouse variation: Implications to the axial ulnar loading protocol and animal specific calibration. J Biomech 46:2271–2276. doi:10.1016/j.jbiomech.2013.06.027

Wallace IJ, Demes B, Mongle C et al (2014) Exercise-induced bone formation is poorly linked to local strain magnitude in the sheep tibia. PLoS ONE 9:e99108. doi:10.1371/journal.pone.0099108

Wang B, Zhou X, Price C et al (2013) Quantifying load-induced solute transport and solute-matrix interaction within the osteocyte lacunar-canalicular system. J Bone Miner Res 28:1075–1086. doi:10.1002/jbmr.1804

Weatherholt AM, Fuchs RK, Warden SJ (2013) Cortical and trabecular bone adaptation to incremental load magnitudes using the mouse tibial axial compression loading model. Bone 52:372–379. doi:10.1016/j.bone.2012.10.026

Weinbaum S, Cowin SC, Zeng Y (1994) A model for the excitation of osteocytes by mechanical loading-induced bone fluid shear stresses. J Biomech 27:339–360. doi:10.1016/0021-9290(94)90010-8

Wergedal JE, Sheng MH-C, Ackert-Bicknell CL et al (2005) Genetic variation in femur extrinsic strength in 29 different inbred strains of mice is dependent on variations in femur cross-sectional geometry and bone density. Bone 36:111–122. doi:10.1016/j.bone.2004.09.012

Willie BM, Birkhold AI, Razi H et al (2013) Diminished response to in vivo mechanical loading in trabecular and not cortical bone in adulthood of female C57Bl/6 mice coincides with a reduction in

deformation to load. Bone 55:335–346. doi:10.1016/j.bone.2013.04.023

Yang H, Butz KD, Duffy D et al (2014) Characterization of cancellous and cortical bone strain in the in vivo mouse tibial loading model using microCT-based finite element analysis. Bone 66:131–139. doi:10.1016/j.bone.2014.05.019

You L, Cowin SC, Schaffler MB, Weinbaum S (2001) A model for strain amplification in the actin cytoskeleton of osteocytes due to fluid drag on pericellular matrix. J Biomech 34:1375–1386

Zeng Y, Cowin SC, Weinbaum S (1994) A fiber matrix model for fluid flow and streaming potentials in the canaliculi of an osteon. Ann Biomed Eng 22:280–292. doi:10.1007/BF02368235

Zhang P (2006) Diaphyseal bone formation in murine tibiae in response to knee loading. J Appl Physiol 100:1452–1459. doi:10.1152/japplphysiol.00997.2005